XXI Simposio CEA de Control Inteligente

24-26 de junio de 2026, Salamanca

Neural Surrogate-Based Operating-Window Identification for Slit-Die Extrusion

Gorakifard, Mohsen[a,b,*], Sierra, Jesus Enrique[a,b], Kian Far, Ehsan[c]

[a]*Department of Digitalization, University of Burgos, C/ Villadiego s/n, 09006 Burgos, Spain.*
[b]*UBU-MICHELIN Joint Research Unit in Automation and Smart Industry, Arainnnov Michelin Aranda, 09400 Aranda de Duero, Spain.*
[c]*Siemens Digital Industries Software, Lake View Dr, Nottingham NG15 0ED, United Kingdom.*

To cite this article: Gorakifard, M., Sierra, J. E., Kian Far, E. 2026. Neural Surrogate-Based Operating-Window Identification for Slit-Die Extrusion. Simposio CEA de Control Inteligente 00, 1-4.

Abstract

Slit-die extrusion requires the simultaneous control of pressure drop, wall shear rate, apparent viscosity, and post-die swell. This work presents a neural surrogate-based workflow for identifying feasible operating windows in slit-die extrusion. A structured synthetic dataset was generated using a reduced-order physics model that combines generalized-Newtonian slit flow, temperature-dependent Carreau–Yasuda rheology, and an empirical area-swell closure. An ensemble of independently initialized multi-output neural networks was trained to predict pressure drop, apparent viscosity, wall shear rate, and area swell ratio, while a separate ensemble of neural classifiers was used to classify feasible and non-feasible operating conditions under pressure, shear-rate, and swell constraints. The regression ensemble achieved R^2 values above 0.9988 for all outputs, and the feasibility classifier reached an accuracy of 0.9838 and an F1-score of 0.9884. The trained models screened 50000 candidate conditions, identified feasible operating windows, and verified the top recommendations against the reduced-order physics solver. The results show that neural surrogate learning can provide a fast decision-support tool for constrained operating-window exploration in extrusion process design.

Keywords: Slit-die extrusion, Neural surrogate, Operating-window identification, Feasibility classification, Digital twin

Identificación de ventanas operativas mediante sustitutos neuronales para la extrusión con matriz de ranura

Resumen

La extrusión con matriz de ranura requiere el control simultáneo de la caída de presión, la tasa de cizalla en pared, la viscosidad aparente y el hinchamiento posterior a la salida. Este trabajo presenta un flujo de trabajo basado en sustitutos neuronales para identificar ventanas operativas factibles. Se generó una base de datos sintética mediante un modelo físico reducido que combina flujo generalizado-newtoniano en ranura, reología Carreau–Yasuda dependiente de la temperatura y una clausura empírica para el hinchamiento de área. Se entrenó un conjunto de redes neuronales multi-salida inicializadas independientemente para predecir las principales variables del proceso, mientras que un conjunto separado de clasificadores neuronales clasificó condiciones factibles y no factibles bajo restricciones de presión, cizalla e hinchamiento. El modelo de regresión alcanzó valores de R^2 superiores a 0.9988, y el clasificador obtuvo una exactitud de 0.9838 y un F1-score de 0.9884. Los modelos evaluaron 50000 condiciones candidatas, identificaron ventanas operativas factibles y verificaron las mejores recomendaciones con el modelo físico reducido. Los resultados muestran que los sustitutos neuronales pueden proporcionar una herramienta rápida de apoyo a la decisión para la exploración restringida de ventanas operativas en extrusión.

Palabras clave: Extrusión con matriz de ranura, Sustituto neuronal, Identificación de ventanas operativas, Clasificación de factibilidad, Gemelo digital

*Corresponding author: mgorakifard@ubu.es
Attribution-NonCommercial-ShareAlike 4.0 International (CC BY-NC-SA 4.0)

1. Introduction

Slit-die extrusion is a key operation in polymer and rubber processing, where it is used to manufacture films, sheets, profiles, seals, and other continuous products. In tire manufacturing and related industrial sectors, extrusion quality is strongly linked to the stability of the operating conditions and to the ability to control the geometry of the extrudate after leaving the die (Gorakifard et al., 2026). From a modelling perspective, slit-die extrusion is governed by the interaction between flow rate, die geometry, temperature, rheology, pressure development, and material-dependent shear-thinning behavior (Baird and Collias, 2014; Michaeli, 2003; Tadmor and Gogos, 2013). Therefore, rapid identification of suitable operating conditions is important for process design, production support, and reduction of trial-and-error adjustments.

A central difficulty is that acceptable operation is not defined by a single process variable. High throughput is desirable, but it may increase pressure drop and wall shear rate. At the same time, post-die deformation may lead to extrudate swell, which affects dimensional accuracy and depends on shear history, wall stress, temperature, die geometry, and material formulation (Müllner et al., 2007; Liang, 2004; Ganvir et al., 2011; Tang et al., 2020). As a result, the practical task is not only to predict pressure, viscosity, shear rate, or swell independently, but to identify regions of the operating space where all relevant constraints are simultaneously satisfied.

Detailed numerical simulations and advanced computational methods can provide valuable insight into complex flow, transport, and interfacial phenomena. Lattice-Boltzmann-based and meshless formulations, for example, have been used to analyze demanding flow problems (Gorakifard et al., 2021, 2022; Kian Far et al., 2023). However, such approaches may be computationally demanding when the objective is to screen thousands of candidate extrusion conditions. This motivates the use of reduced-order physical models and data-driven approximations for rapid scenario exploration, especially when the goal is operating-window identification rather than full-field resolution.

Machine-learning surrogate models provide an efficient route for accelerating process analysis and optimization. In polymer extrusion, surrogate and artificial-intelligence approaches have been applied to prediction, process optimization, and data-driven support using computational or digital-twin-generated data (Sarishvili et al., 2021; Gaspar-Cunha et al., 2022b,a; Polychronopoulos et al., 2025). Recent studies have also considered inverse recommendation and robust operating-condition search for extrusion-related continuous manufacturing processes (Burr et al., 2023; Cruz-Oliver et al., 2024). These works show the growing importance of moving from isolated prediction toward decision-support methods. Nevertheless, operating-window identification remains challenging because the model must evaluate multiple process constraints and rank candidate conditions according to engineering objectives.

This work presents a neural surrogate-based workflow for operating-window identification in slit-die extrusion. The contribution is threefold. First, a reduced-order slit-flow model is used to generate a structured synthetic dataset linking operating conditions, material descriptors, and geometry to pressure drop, apparent viscosity, wall shear rate, and area swell ratio. Second, an ensemble of independently initialized multi-output neural networks is developed to predict these coupled process responses simultaneously, while a separate ensemble of neural classifiers maps candidate conditions into feasible and non-feasible regions under pressure, shear-rate, and swell constraints. Third, the trained neural models are embedded in a search-and-ranking procedure that identifies candidate operating windows and verifies the best recommendations against the reduced-order physics solver. In this way, the proposed framework moves beyond response prediction and provides a fast decision-support tool for constrained operating-window exploration in extrusion process design.

2. Methodology

The proposed workflow combines reduced-order physics, neural surrogate learning, feasibility classification, and constrained operating-window search. For each scenario, the neural-network input vector includes the operating variables, material descriptors, and engineered geometric and operating features. The operating variables are the material temperature T, slit width W, slit height H, die-land length L, and volumetric flow rate Q. The material descriptors include the material class, the Carreau–Yasuda parameters $\eta_{0,\mathrm{ref}}$, $\eta_{\infty,\mathrm{ref}}$, n, a, and λ_{ref}, the activation energy E, the filler factor, the density, and the swell-strength parameter. Additional geometric and operating features are computed as

$$D_{\mathrm{eq}} = \frac{2WH}{W+H}, \qquad \frac{L}{H}, \qquad \frac{W}{H}, \qquad \frac{L}{D_{\mathrm{eq}}}, \qquad \frac{Q}{WH}. \tag{1}$$

Logarithmic geometry and flow-rate features, temperature-shift terms, and interaction terms involving temperature, filler factor, and viscosity are also included. Numerical features are standardized before training, while the material class is one-hot encoded. A structured synthetic database is generated by sampling bounded operating ranges and perturbing representative material classes.

The dataset included four representative material classes: low-filled EPDM, medium-filled EPDM, high-filled EPDM, and a reprocessed compound. The operating variables were sampled within the ranges summarized in Table 1. In addition, 25% of the samples were generated using boundary-focused sampling to improve learning near the limits of the design space.

Table 1: Operating-variable ranges used for synthetic dataset generation.

Variable	Description	Range
T	Material temperature	363.15–423.15 K
W	Slit width	0.015–0.080 m
H	Slit height	0.0010–0.0050 m
L	Die-land length	0.005–0.040 m
Q	Volumetric flow rate	1.5×10^{-7}–9.5×10^{-6} m^3/s

After solving the reduced-order physics model, samples were retained only if they satisfied numerical-consistency and physical-admissibility criteria, including positive flow rate, wall shear rate, apparent viscosity, wall stress, pressure drop, residence time, and mass flow rate; bounded pressure, viscosity, shear rate, residence time, mean velocity, and swell ratio; and a relative flow-rate solver error below 5×10^{-4}.

The reduced-order physical core is based on fully developed generalized-Newtonian slit flow. Temperature dependence is introduced through an Arrhenius shift factor,

$$a_T = \exp\left[\frac{E}{R}\left(\frac{1}{T} - \frac{1}{T_{\text{ref}}}\right)\right], \tag{2}$$

which modifies the Carreau–Yasuda parameters as $\eta_0(T) = \eta_{0,\text{ref}} a_T$, $\eta_\infty(T) = \eta_{\infty,\text{ref}} a_T$, and $\lambda(T) = \lambda_{\text{ref}} a_T$. The apparent viscosity is given by

$$\eta(\dot{\gamma}, T) = \eta_\infty(T) + [\eta_0(T) - \eta_\infty(T)]\,(1 + [\lambda(T)\dot{\gamma}]^a)^{(n-1)/a}. \tag{3}$$

For a trial wall stress τ_w, the local shear rate is obtained from $\tau(y) = \eta(\dot{\gamma}, T)\dot{\gamma}$, and the wall stress is found by enforcing $Q_{\text{calc}}(\tau_w) - Q = 0$. The pressure drop is then computed as

$$\Delta P_{\text{land}} = \frac{2L\tau_w}{H}. \tag{4}$$

Post-die deformation is represented by an empirical area-swell closure separated from the in-die transport model:

$$B_A = 1 + S\, g_\gamma g_\tau g_L g_F g_T \tag{5}$$

where g_γ, g_τ, g_L, g_F, and g_T account for wall shear rate, wall stress, die geometry, filler factor, and temperature, respectively. This separation preserves the distinction between in-die flow prediction and post-die recovery.

An ensemble of independently initialized multi-output multilayer perceptrons is trained to emulate the reduced-order model using the input vector described above. Here, η_w denotes the apparent viscosity evaluated at the wall shear rate, and $\dot{\gamma}_w$ denotes the wall shear rate. The output vector is

$$\mathbf{y} = [\Delta P_{\text{land}}, \eta_w, \dot{\gamma}_w, B_A]. \tag{6}$$

Logarithmic transformations are applied to the regression targets to improve numerical conditioning. The regression surrogate consists of three independently initialized multilayer perceptrons. Each network has four hidden layers with 192, 128, 64, and 32 neurons, respectively, uses rectified linear unit activation functions, and is trained with the Adam optimizer. Each network predicts the four outputs in Eq. (6) simultaneously. The final surrogate prediction is obtained as the ensemble mean, while the dispersion among the three independently trained networks is used as a prediction-uncertainty indicator.

A separate neural ensemble is trained as a feasibility classifier. This classifier ensemble consists of three independently initialized multilayer perceptrons with hidden layers of 128, 64, and 32 neurons, respectively. Each classifier predicts the probability that a candidate condition is feasible, and the final feasibility probability is obtained by averaging the three classifier outputs. A condition is labelled feasible if

$$\Delta P_{\text{land}} \le \Delta P_{\max}, \qquad \dot{\gamma}_w \le \dot{\gamma}_{\max}, \qquad B_{A,\min} \le B_A \le B_{A,\max}. \tag{7}$$

The limits are set to $\Delta P_{\max} = 2.0 \times 10^8$ Pa, $\dot{\gamma}_{\max} = 800\ \text{s}^{-1}$, $B_{A,\min} = 1.03$, and $B_{A,\max} = 1.25$. The classifier threshold is optimized on a validation subset.

Finally, a large set of candidate operating conditions is generated within the admissible design space. The neural regressors predict the process responses, the classifier estimates feasibility, and feasible candidates are ranked using an objective that rewards high throughput, pressure and shear-rate margins, swell proximity to the target interval, high feasibility probability, and low ensemble uncertainty. The highest-ranked candidates are re-evaluated with the reduced-order physics solver to verify the neural recommendations. The ranking objective was defined as a weighted score combining normalized throughput, pressure margin, shear-rate margin, swell proximity to the target interval, feasibility probability, and ensemble uncertainty:

$$J = 0.35S_Q + 0.20S_P + 0.15S_\gamma + 0.20S_B + 0.10p_f - 0.15U,$$

where S_Q is the normalized flow-rate score, S_P and S_γ are the pressure and shear-rate margin scores, S_B measures the proximity of B_A to the centre of the admissible swell interval, and p_f is the ensemble feasibility probability. The uncertainty term U is computed from the relative ensemble standard deviations of pressure drop, wall shear rate, and swell ratio. Therefore, candidates with higher ensemble dispersion are penalized linearly in the final ranking score.

3. Results and discussion

The proposed workflow generated 8000 physically admissible synthetic scenarios after numerical filtering. According to the feasibility definition introduced in Eq. (7), 69.8% of the generated scenarios were classified as feasible. This distribution indicates that the sampled design space contains both acceptable and non-acceptable operating conditions, allowing the neural classifier to learn a meaningful separation between feasible and infeasible regions.

The multi-output neural ensemble reproduced the reduced-order physics outputs with high accuracy on the held-out test set. As shown in Table 2, all predicted variables reached R^2 values above 0.9988. The best agreement was obtained for wall shear rate and area swell ratio, while pressure drop and apparent viscosity also showed excellent predictive performance. These results indicate that the neural ensemble captures the coupled relation between operating variables, material descriptors, geometry, and the reduced-order extrusion responses.

Table 2: Performance of the multi-output neural ensemble on the held-out test set.

Variable	MAE	RMSE	R^2
ΔP_{land}	6.97×10^5	1.52×10^6	0.9991
η_w	4.23×10^2	1.12×10^3	0.9989
$\dot{\gamma}_w$	1.86	7.24	0.9996
B_A	1.28×10^{-3}	1.68×10^{-3}	0.9995

Figure 1 shows the parity plots between the reduced-order physics outputs and the neural predictions. The points are concentrated around the identity line for all four outputs, confirming that the neural ensemble provides an accurate approximation of the physics-generated response surface. The agreement for pressure drop and wall shear rate is especially important because these variables define the mechanical loading of the extrusion process, while the accurate prediction of B_A supports the use of the model for dimensional-quality screening.

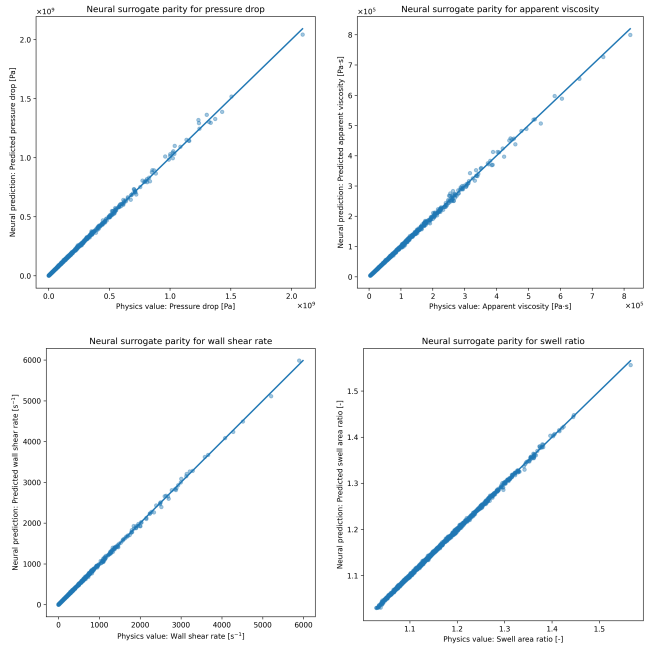


Figure 1: Parity plots comparing reduced-order physics outputs and neural ensemble predictions for pressure drop, apparent viscosity, wall shear rate, and area swell ratio.

The feasibility classifier also achieved strong performance. As summarized in Table 3, the optimized classifier reached an accuracy of 0.9838 and an F1-score of 0.9884 on the held-out test set. The confusion matrix contained 471 true negatives, 1103 true positives, 12 false positives, and 14 false negatives. This result shows that the classifier can reliably distinguish feasible and non-feasible operating conditions under simultaneous pressure, shear-rate, and swell constraints. Although the optimized threshold of 0.570 maximizes the validation F1-score, the subsequent operating-window search applies a more conservative minimum feasibility probability of 0.70 for candidate recommendation. Thus, a candidate is recommended only if its ensemble feasibility probability satisfies $p_f \geq \max(0.570, 0.70)$, in addition to satisfying the explicit pressure, wall-shear-rate, and swell constraints. This conservative filtering reduces the likelihood of false-positive feasible recommendations and provides an additional safety margin for industrial applications.

Table 3: Performance of the neural feasibility classifier on the held-out test set.

Metric	Value
Optimized threshold	0.570
Accuracy	0.9838
Precision	0.9892
Recall	0.9875
F1-score	0.9884

After training, the neural ensembles were used to evaluate 50000 candidate operating conditions. The search identified 34515 feasible candidates satisfying the imposed process constraints. Figure 2 presents the recommended feasible region in terms of predicted pressure drop and predicted area swell ratio, with the volumetric flow rate represented by color. The figure shows that the method provides a practical map of acceptable operating conditions, rather than only isolated response predictions. This is useful for selecting conditions that remain within admissible pressure and swell limits while maintaining desirable throughput.

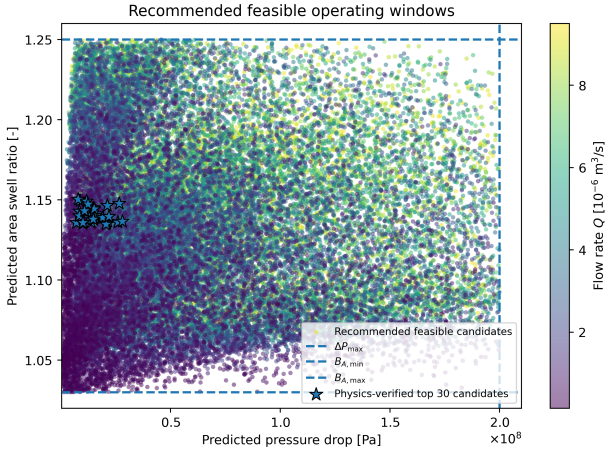


Figure 2: Recommended feasible operating windows obtained from the neural ensemble search. Color represents the volumetric flow rate. The dashed lines indicate the feasibility constraints ($\Delta P_{\max} = 2.0 \times 10^8$ Pa, $B_{A,\min} = 1.03$, and $B_{A,\max} = 1.25$), while the star markers denote the physics-verified top 30 candidates.

A computational benchmark was performed to compare operating-window screening using the neural surrogate workflow and the reduced-order physics solver. Screening 50000 candidate operating conditions required 2.13 s using the trained neural ensembles, whereas direct evaluation with the reduced-order physics solver required 54275 s (approximately 15.1 h) on the same computational platform. This corresponds to an acceleration factor of approximately 2.55×10^4 (approximately 25 500× faster). The benchmark excludes neural-network training time and includes prediction together with feasibility filtering. These results support the use of the proposed framework as a rapid decision-support tool for operating-window exploration.

To verify the reliability of the neural recommendations, the highest-ranked operating windows were re-evaluated using the reduced-order physics solver. Table 4 summarizes the verification errors for the top 30 recommended candidates. The mean relative errors were 1.14% for pressure drop, 1.16% for apparent viscosity, and 1.64% for wall shear rate. The mean absolute error in swell ratio was 1.33×10^{-3}. These small discrepancies confirm that the neural search does not generate recommendations that are inconsistent with the underlying physics model.

Table 4: Physics verification of the top 30 neural operating-window recommendations.

Verification metric	Value
Mean relative error in ΔP_{land}	1.14%
Mean relative error in η_w	1.16%
Mean relative error in $\dot{\gamma}_w$	1.64%
Mean absolute error in B_A	1.33×10^{-3}
Max. relative error in ΔP_{land}	3.39%
Max. absolute error in B_A	3.59×10^{-3}

Overall, the results show that the proposed neural workflow is suitable for rapid operating-window exploration. The multi-output neural ensemble provides accurate response prediction, the classifier gives a reliable feasibility map, and the search procedure identifies operating candidates that satisfy multiple

constraints simultaneously. Compared with a pure response-prediction surrogate, this formulation is more useful for process decision support because it directly connects prediction, feasibility assessment, candidate ranking, and physics-based verification.

4. Conclusions

This work presented a neural surrogate-based workflow for operating-window identification in slit-die extrusion. A structured synthetic dataset was generated using a reduced-order physics model that combines generalized-Newtonian slit flow, temperature-dependent Carreau–Yasuda rheology, and an empirical area-swell closure. The dataset was used to train an ensemble of independently initialized multi-output MLP regressors for simultaneous prediction of pressure drop, apparent viscosity, wall shear rate, and area swell ratio, together with a separate ensemble of MLP classifiers for feasible/non-feasible operating-condition identification.

The neural ensemble reproduced the reduced-order physics outputs with high accuracy, reaching R^2 values above 0.9988 for all predicted variables. The feasibility classifier also showed strong performance under simultaneous pressure, shear-rate, and swell constraints, reaching an accuracy of 0.9838 and an F1-score of 0.9884. The trained models were then used to screen 50000 candidate operating conditions and identify feasible operating windows within the admissible design space.

The highest-ranked recommendations were verified using the reduced-order physics solver. The verification showed small discrepancies, with mean relative errors below 1.7% for pressure drop, apparent viscosity, and wall shear rate, and a mean absolute error of 1.33×10^{-3} for the area swell ratio. These results indicate that the proposed approach can move beyond response prediction and provide a fast decision-support tool for constrained operating-window exploration in extrusion process design.

Future work will focus on calibration with experimental extrusion data, extension to additional material families and die geometries, and integration of the neural feasibility map into industrial digital-twin environments for real-time process recommendation. Although the present study relies on synthetic data generated from a reduced-order physics model, the proposed ensemble architecture is compatible with noisy plant measurements. In industrial deployment, retraining or fine-tuning with experimental data, together with ensemble averaging and uncertainty monitoring, could improve robustness against measurement noise and process variability.

Acknowledgements

The authors gratefully acknowledge the computational resources provided by the Centro de Supercomputación de Castilla y León (SCAYLE; `https://www.scayle.es/`).

References

Baird, D. G., Collias, D. I., 2014. Polymer processing: principles and design. John Wiley & Sons.

Burr, J., Sarishvili, A., Just, D., Katsaouni, N., Moser, K., 2023. Plastic extrusion process optimization by inversion of stacked autoencoder classification machines. Chemie Ingenieur Technik 95 (10), 1555–1562.

Cruz-Oliver, R., Monzon, L., Ramirez-Laboreo, E., Rodriguez-Fortun, J.-M., 2024. Rom-based stochastic optimization for a continuous manufacturing process. ISA transactions 154, 242–249.

Ganvir, V., Gautham, B., Pol, H., Bhamla, M. S., Sclesi, L., Thaokar, R., Lele, A., Mackley, M., 2011. Extrudate swell of linear and branched polyethylenes: Ale simulations and comparison with experiments. Journal of non-newtonian fluid mechanics 166 (1-2), 12–24.

Gaspar-Cunha, A., Covas, J. A., Sikora, J., 2022a. Optimization of polymer processing: a review (part i—extrusion). Materials 15 (1), 384.

Gaspar-Cunha, A., Monaco, F., Sikora, J., Delbem, A., 2022b. Artificial intelligence in single screw polymer extrusion: Learning from computational data. Engineering Applications of Artificial Intelligence 116, 105397.

Gorakifard, M., Saluena, C., Cuesta, I., Far, E. K., 2021. Analysis of aeroacoustic properties of the local radial point interpolation cumulant lattice boltzmann method. Energies 14 (5), 1443.

Gorakifard, M., Saluena, C., Cuesta, I., Kian Far, E., 2022. The meshless local petrov–galerkin cumulant lattice boltzmann method: Strengths and weaknesses in aeroacoustic analysis. Acta mechanica 233 (4), 1467–1483.

Gorakifard, M., Sierra, J. E., Kian Far, E., 2026. Polymer extrusion processes in tire manufacturing: a systematic review and bibliometric analysis. The International Journal of Advanced Manufacturing Technology, 1–48.

Kian Far, E., Gorakifard, M., Goraki Fard, M., 2023. A new three dimensional cumulant phase field lattice boltzmann method to study soluble surfactant. Physics of Fluids 35 (5).

Liang, J.-Z., 2004. A relationship between extrudate swell ratio and entry stored elastic strain energy during die flow of tyre compounds. Polymer Testing 23 (4), 441–446.

Michaeli, W., 2003. Extrusion Dies for Plastics and Rubber: Design and Engineering Computations. Hanser Publishers, Munich.

Müllner, H. W., Eberhardsteiner, J., Fidi, W., 2007. Rheological characterization of the die swell phenomenon of rubber compounds. Polymer testing 26 (8), 1041–1048.

Polychronopoulos, N. D., Sarris, I., Vlachopoulos, J., 2025. Implementation of machine learning in flat die extrusion of polymers. Molecules 30 (9), 1879.

Sarishvili, A., Just, D., Moser, K., Wirsen, A., Diemert, J., Jirstrand, M., 2021. Plastic extrusion process optimization by digital twins. Chemie Ingenieur Technik 93 (12), 1949–1954.

Tadmor, Z., Gogos, C. G., 2013. Principles of polymer processing. John Wiley & Sons.

Tang, D., Marchesini, F. H., Cardon, L., D'hooge, D. R., 2020. The impact of upstream contraction flow on three-dimensional polymer extrudate swell from slit dies. Journal of Non-Newtonian Fluid Mechanics 282, 104337.